Low-strain Si/O superlattices with tunable electronic properties: *Ab initio* calculations

Kengo Nishio,[1,*] Anh Khoa Augustin Lu,[2,3] and Geoffrey Pourtois[2,4]
[1]*National Institute of Advanced Industrial Science and Technology (AIST), Central 2, Umezono 1-1-1, Tsukuba, Ibaraki 305-8568, Japan*
[2]*IMEC, 75 Kapeldreef, B-3001 Leuven, Belgium*
[3]*Department of Physics, Katholieke Universiteit Leuven, B-3001 Leuven, Belgium*
[4]*PLASMANT, Department of Chemistry, University of Antwerp, B-2610 Antwerp, Belgium*
(Received 26 May 2014; revised manuscript received 6 March 2015; published 16 April 2015)

We propose that low-strain Si/O superlattices can be constructed by connecting reconstructed Si{001} surfaces by Si-O-Si bridges. *Ab initio* calculations show that our models are energetically more favorable than all the models proposed so far. The part of our Si/O superlattice model is experimentally accessible just by oxidizing a Si(001) substrate. To complete our Si/O superlattice model, we propose a three-step method. We also explore the potential of our Si/O superlattice models for new materials used in future Si electronics. We find that the location of the channel where the carriers travel can be controlled between the interfaces and the Si layers by the insertion of O atoms into the Si-Si dimers. By revealing the origins of the interface electron and hole states, we find that similar interface states should be easily achieved for Si slabs and Si substrates. Interestingly, the interface electrons and holes have small effective masses in the direction parallel to the channel and large effective masses in the direction normal to the channel, which makes the Si/O superlattices attractive to be used for channel materials. We also find that the valley splitting of Si is enhanced by the formation of the Si/O/Si interfaces, which is ideal for developing Si-based qubits. Our findings open new perspectives to design and control the electronic properties of Si.

DOI: 10.1103/PhysRevB.91.165303 PACS number(s): 68.65.Cd, 68.35.−p, 73.20.At, 73.21.Cd

I. INTRODUCTION

Challenges to explore new materials and phenomena are the driving forces to further extend the frontiers of materials science and technology. For instance, for Si-based materials, the discovery of photoluminescence from Si nanostructures has stimulated studies of the impact of quantum confinement effects to tune the light-emitting properties of Si and to realize Si-based optoelectronics [1–10]. Another example is the discovery of piezoresistance in Si and Ge [11], which has stimulated the investigation of the effects of strain on the electronic transport properties of Si [12–15]. Nowadays, strained Si is commonly used to enhance the performance of Si-based transistors [13]. Recently, the impact of computer simulations to offer guidelines in the identification of potentially useful new materials has been increasing [14–21]. For example, silicene was first predicted by *ab initio* calculations [19] and then later on realized experimentally [20,21].

The idea of exploiting semiconductor atomic superlattices (SLs), which are composed of alternate epitaxial semiconductor layers and atomically thin layers of adsorbed atoms, was proposed by Tsu to control quantum confinement effects [22–24]. Recently, the Si/O SL concept has been gaining momentum and is expected to provide a new opportunity to improve the electronic transport properties of Si [25,26]. The epitaxial growth of Si on an O monolayer adsorbed on a Si(001) substrate and the resulting epitaxial Si/O SLs have been demonstrated [24–26]. However, given their complex nature, the atomic structure of the Si/O/Si interfaces has not been thoroughly resolved experimentally and remains a mystery. The identification of the most stable structures of the Si/O/Si interface would be valuable for optimizing the growth conditions and tailoring their electronic transport properties. Several structure models of the Si/O SL have already been proposed [23,27]. However, these have large formation energies and suffer from large strains as discussed later.

In this paper, we theoretically explore the most stable structures of the Si/O SL and propose a method to realize them experimentally. Our *ab initio* calculations show that low-energy and low-strain Si/O SLs can be constructed by connecting reconstructed Si{001} surfaces [28] by Si-O-Si bridges. The part of our Si/O SL model has already been realized experimentally. By extending the technique, we propose a three-step method to complete our Si/O SL model. We also explore the potential of our Si/O SL models for new materials used in future Si electronics. Interestingly, our Si/O SL models have unique electronic properties such as the tunable channel location, small carrier effective masses, and large valley splitting, which makes them attractive materials for advanced Si electronics.

II. LOW-STRAIN STRUCTURE

A. Geometrical consideration

Our strategy for constructing the Si/O SL models consists in connecting the reconstructed Si{001} surfaces by the Si-O-Si bridges, as illustrated in Fig. 1(a) (Rec-I interface). This Si/O/Si interface has the following five geometrical features, which allow each atom to maintain its natural bonding configuration.

(i) The arrangement of the Si atoms involved in the Si/O/Si interface is intrinsic to Si, so that the interface does not induce a large strain in the Si layers.

(ii) All the dangling bonds of the Si-Si dimers are passivated by the Si-O-Si bridging bonds.

*k-nishio@aist.go.jp

 ©2015 American Physical Society

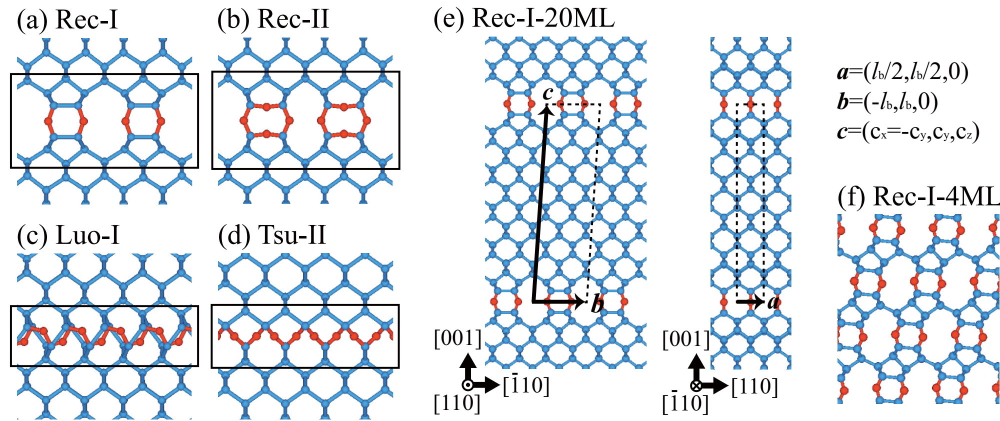

FIG. 1. (Color online) Atomic arrangement. (a) Rec-I, (b) Rec-II, (c) Luo-I, and (d) Tsu-II Si/O/Si interface models. Blue and red (light and dark gray) particles are Si and O atoms, respectively. Blue and red (light and dark gray) bonds are Si-Si and Si-O bonds, respectively. Framed regions define the Si/O/Si interfaces to evaluate the lattice mismatches of the interfaces with Si. (e) Epitaxial Rec-I-20ML SL. The dashed lines show the unit cell. The arrows are the unit-cell vectors: ***a***, ***b***, and ***c***. (f) Freestanding Rec-I-4ML SL.

(iii) The Si-O bond lengths and O-Si-Si bond angles can be tuned to their optimal values by adjusting the positions of the O atoms and the distance between the Si surfaces.

(iv) The Si-O-Si bond angles can adapt themselves to a geometry determined by the optimal Si-O bond lengths and the O-Si-Si bond angles because of the flexibility of the Si-O-Si bridging bonds.

(v) The oxidation state of the interface Si atoms can be tuned by inserting additional O atoms into the Si-Si dimers, as illustrated in Fig. 1(b) (Rec-II interface), without inducing a large strain since the oxygen inserted dimers (Si-O-Si dimers) are energetically favorable structures [29].

For comparison purpose, interface models proposed by Luo *et al.* [27] and Tsu *et al.* [23], hereafter referred to as the Luo-I and Tsu-II models, are illustrated in Figs. 1(c) and 1(d), respectively. Here, I (II) indicates the oxidation state of the forefront Si atoms +1 (+2). Note that the area densities of the O atoms for the Rec-I and Luo-I (Rec-II and Tsu-II) are 2 (4) atoms per l_b^2, where l_b is the lattice constant of bulk Si: 5.460 Å in our simulation scheme (see the Supplemental Material for details [30]).

B. *Ab initio* calculation

To qualitatively investigate the stabilities of the SLs, we carried out *ab initio* calculations using the QMAS code [31]. The QMAS code is based on the density functional theory (DFT) with the generalized gradient approximation (GGA) [32] and the projector-augmented-wave method [33]. The plane-wave cut-off energy was set to 50 Ry. The convergence criteria of 5×10^{-5} Hartree/Bohr for forces on atoms and 3×10^{-7}Hartree/Bohr^3 for the stress components were used. $8 \times 4 \times 4$, $8 \times 4 \times 2$, and $8 \times 4 \times 2$ k-point grids were used for 4 ML, 20 ML, and 40 ML SLs, respectively.

We first optimized the structures of the epitaxial Rec-I-20ML [Fig. 1(e)], Rec-II-20ML, Luo-I-20ML, and Tsu-II-20ML SLs. Here, 20 ML indicates the number of Si monolayers (MLs) in each Si layer. Although the interface between the Si substrate and the Si/O SL was not included in a unit cell, the in-plane unit-cell vectors ***a*** and ***b*** of the epitaxial Si/O SL were constrained to match the Si(001) substrate (see the Supplemental Material for details [30]). On the other hand, the out-of-plane vector ***c*** and all the atomic positions were optimized to minimize the total energy. Note that the a and b axes were set to be along the [110] direction normal to the Si-Si dimers and the [$\bar{1}$10] direction parallel to the Si-Si dimers, respectively.

We compare the stabilities of the Si/O SLs in terms of their formation energies per O atom:

$$f \equiv (E_{\mathrm{tot}} - n_{\mathrm{Si}}\mu_{\mathrm{Si}} - n_{\mathrm{O}}\mu_{\mathrm{O}})/n_{\mathrm{O}}.$$

Here, E_{tot} is the total energy per unit cell containing n_{Si} Si atoms and n_{O} O atoms. The chemical potentials μ_{Si} and μ_{O} correspond to the energies per atom calculated for bulk Si and for the O_2 molecules, respectively. The results summarized in Table I demonstrate that our Rec-I-20ML (Rec-II-20ML) model is more stable by 0.60 (1.05) eV/atom than the Luo-I-20ML (Tsu-II-20ML) model.

To further demonstrate the advantages of our models, we investigate the strain present in the Si/O SLs. The lattice mismatches are often used as a measure of the strain in a SL composed of materials having the same crystal structure.

TABLE I. Formation energies and lattice mismatches calculated for the different models. $\epsilon_a \equiv (a - a_{\mathrm{b}})/a_{\mathrm{b}}$. a and b are the lengths of the in-plane cell vectors. γ is the angle made between ***a*** and ***b***. a_{b}, b_{b}, and γ_{b} are the values for bulk Si: $\sqrt{2}l_{\mathrm{b}}/2$, $\sqrt{2}l_{\mathrm{b}}$, and 90°, respectively.

	f (eV/atom)	ϵ_a (%)	ϵ_b (%)	ϵ_γ (%)
epitaxial Rec-I-20ML	−3.62	–	–	–
epitaxial Luo-I-20ML	−3.02	–	–	–
epitaxial Rec-II-20ML	−4.08	–	–	–
epitaxial Tsu-II-20ML	−3.03	–	–	–
freestanding Rec-I-4ML	−3.67	0.0	−1.5	0.0
freestanding Luo-I-4ML	−3.19	−0.2	8.6	0.0
freestanding Rec-II-4ML	−4.09	2.5	2.7	0.0
freestanding Tsu-II-4ML	−3.52	4.9	4.9	−18.6

For Si/O SLs, however, the lattice mismatches are not well defined because the atomically thin O layer does not have a corresponding bulk structure. Accordingly, instead of calculating the lattice mismatches of O with Si, we calculated those of the Si/O/Si interfaces with Si. For this purpose, we define the Si/O/Si interfaces as the framed regions illustrated in Figs. 1(a)–1(d). The lattice mismatches of the Si/O/Si interface can be captured by its corresponding 4 ML SL constructed by stacking the interfaces. To quantify the lattice mismatches of the interfaces, the lattice parameters of the freestanding Rec-I-4ML [Fig. 1(f)], Rec-II-4ML, Luo-I-4ML, and Tsu-II-4ML SLs were calculated by optimizing all the unit-cell vectors without applying any constraint. Note that freestanding indicates that the SL is not grown on a Si substrate. The results are summarized in Table I together with their corresponding formation energies. The lattice mismatches of the Rec-I and Rec-II interfaces are at most 2.7%. On the other hand, the Luo-I interface has a mismatch of 8.6% along the b direction. This originates from the fact that the O atoms are forced into Si-Si bonds of the diamond structure. The Tsu-II interface has a mismatch of -18.6% in the angle made between the $\boldsymbol{a}$ and $\boldsymbol{b}$ unit-cell vectors. This large distortion originates from the fact that the O-Si-O bond of the interface Si atom is twisted around the angle bisector of the Si-Si-Si bond to connect the nonreconstructed Si$\{001\}$ surfaces by the Si-O-Si bridges. These results demonstrate that our Si/O/Si interfaces offer better epitaxial matches with Si than the interfaces proposed so far.

C. Clue to the experimental realization

The part of the Rec-II interface is experimentally accessible [34–37]. Actually, when a Si(001) substrate is oxidized, an atomically thin tridymite (t-SiO_2) layer can form between the Si and amorphous SiO_2 (a-SiO_2). The structure of the Si/t-SiO_2 interface resembles to that of the Rec-II interface in the sense that it contains the Si-O-Si dimers and that the dangling bonds of the dimers are passivated by the Si-O-Si bridging bonds. Note that although a Si/t-SiO_2 structure model composed of Si-Si dimers were considered in the original study of Ourmazd [34], the Si-O-Si dimers would be energetically more favorable [29,35–37]. The whole Rec-II interface should be obtained by a three-step method as follows:

(i) oxidation of a Si(001) to form the Si/t-SiO_2/a-SiO_2 structure,

(ii) hydrofluoric acid treatment to remove needless t-SiO_2 and a-SiO_2,

(iii) epitaxial growth of Si to complete the Rec-II interface.

Finally, the Rec-II SL can be obtained by repeating the three-step method. Note that in step (i) the thickness of SiO_2 layer may be important because it is proposed that a Si/cristobalite (c-SiO_2) interface forms at the initial stage of oxidation and the c-SiO_2 layer transforms to the t-SiO_2 layer to release compressive strains as the oxidation proceeds [34,37,38].

In addition to the epitaxial growth, our Si/O SL models should be accessible by a solution-phase synthesis using hydrolysis of OH-terminated Si membranes [39] because our Si/O SLs are energetically more favorable without the Si(001) substrate than the SLs proposed so far (Table I).

III. UNIQUE ELECTRONIC PROPERTIES

To explore the unique electronic properties, we calculated the electronic states of the epitaxial Rec-I and Rec-II SLs using the OpenMX code [40]. The OpenMX code is based on the DFT with the GGA [32] and the norm-conserving pseudopotentials [41]. The wave functions (WFs) are expressed by the linear combination of pseudoatomic orbitals. The basis sets, Si7.0-$s3p3d2$, O5.0-$s3p3d2$, and H5.0-$s3p3$ were used for Si, O, and H atoms, respectively, except for the 40ML SLs where Si7.0-$s2p2d1$ and O5.0-$s2p2d1$ were used. Here, the abbreviation, for example Si7.0-$s3p3d2$, indicates that three s, three p, and two d orbitals of a Si atom with the cut-off radius of 7.0 Bohr were employed. The effective masses were calculated from the band structures obtained by a noncollinear DFT including the spin-orbit coupling [42–44], while the WFs were calculated by a spin-unpolarized scheme. $16 \times 8 \times 8$, $16 \times 8 \times 2$, and $16 \times 8 \times 2$ k-point grids were used for 4ML, 20ML and 40ML Si/O SLs, respectively.

A. Tunability of the location of the channel

Figure 2 shows the band structures and isosurfaces of the WFs of our SLs. For comparison, we provide the corresponding band structure and WFs of bulk Si in Appendix A. The most remarkable feature of our SLs is the tunability of the location of the channel where the electrons or holes travel. The WF of the C_{I} level of the Rec-I-20ML SL, which is the bottom of the first lowest conduction band (CB1), is localized around the Si/O/Si interfaces. On the other hand, the WF of the V_a level, which is the top of the first highest valence band (VB1), delocalizes over the Si layers. To our surprise, the situation is reversed in the Rec-II-20ML SL. The VB1-top V_{II} level is the interface state, while the WF of the CB1-bottom $\Delta_{2\Gamma}$ level delocalizes over the Si layers. The same behaviors are also found in the Rec-I- and Rec-II-40ML SLs (Appendix B). We also show the WFs of a Si/O SL composed of alternating Rec-I and Rec-II interfaces in Fig. 2(e). The CB1-bottom WF is localized around the Rec-I interface, while the VB1-top WF is localized around the Rec-II interface. Furthermore, the interface states are also found in isolated slab models (Appendix C). Altogether, the location of the channel can be controlled between the Si/O/Si interfaces and the Si layers by the interface structure.

Note that although the d orbitals are mixed a little, the Rec-I interface state mainly consists of s, p_b, and p_z orbitals. On the other hand, the Rec-II interface state consists of almost p_a orbitals only.

B. Origin of interface electron state

The Rec-I interface electron state primarily originates from the interactions between the adjacent Si layers. This is verified by the fact that the interface electron state also occurs in a pile of Si slabs with H-terminated Si-Si dimers [Fig. 3(a)]. According to a previous study, the energy gap of SiO_2 close to the Si/SiO_2 interface is almost the same as the band gap of Si [36]. Similarly, the Si/O/Si interfaces, corresponding to atomically thin suboxide layers, are not good insulators. Therefore, the WF can penetrate through the Si/O/Si interface, and the electronic states of the adjacent Si layers can couple each other.

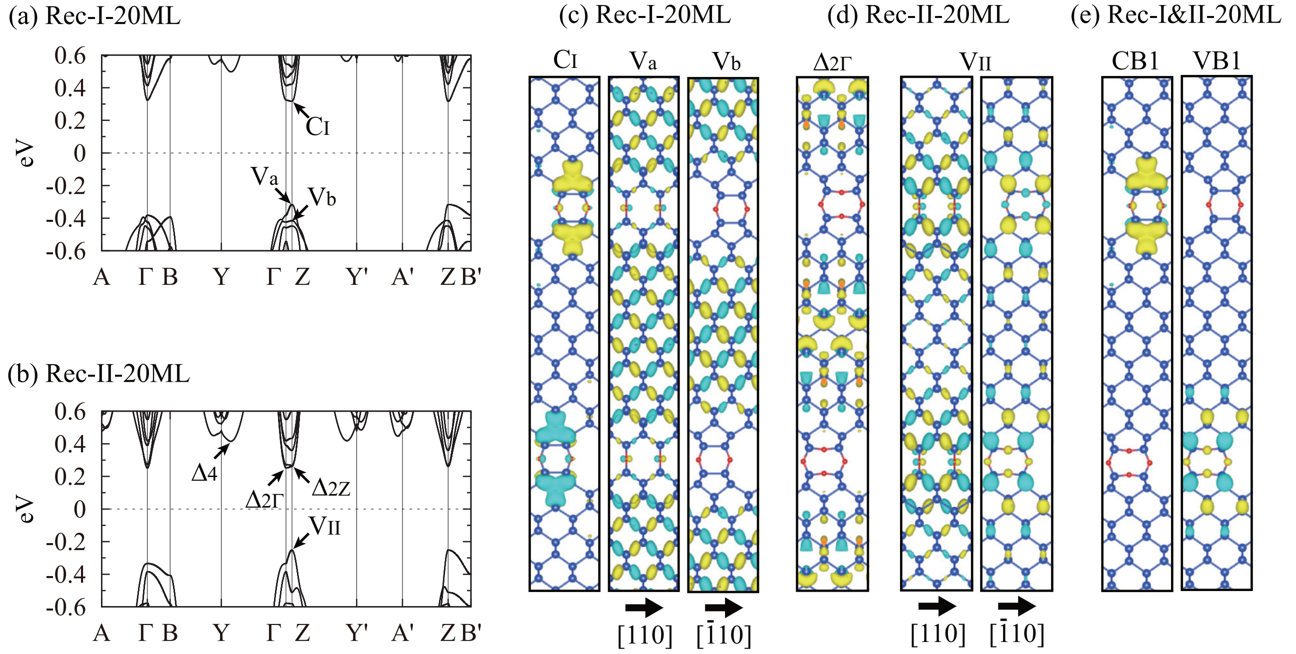

FIG. 2. (Color) Electronic structures of the epitaxial SLs. The band structures of (a) Rec-I- and (b) Rec-II-20ML SLs. Note that the energy is measured from the Fermi level. A $= \frac{2\pi}{l_b}(\frac{1}{2},\frac{1}{2},0) \equiv [\frac{1}{2},\frac{1}{2},0]$, $\Gamma = [0,0,0]$, B $= [-\frac{1}{4},\frac{1}{4},0]$, Y $= [0,1,0]$, Z $= [0,0,\frac{l_b}{2c_z}]$, Y$' = [0,1,\frac{l_b}{2c_z}]$, A$' = [\frac{1}{2},\frac{1}{2},\frac{l_b}{2c_z}]$, and B$' = [-\frac{1}{4},\frac{1}{4},\frac{l_b}{2c_z}]$. These points are not necessarily in the first Brillouin zone. l_b and c_z are the lattice constant of bulk Si and z component of out-of-plane unit cell-vector $\boldsymbol{c}$ (See also Fig. 1). (c) The isosurfaces (± 0.020 in units of electron$^{1/2}/a_0^{3/2}$) of WFs of the C_I, V_a, and V_b levels of the Rec-I-20ML SL. Here, a_0 is the Bohr radius. (d) The isosurfaces of WFs of the $\Delta_{2\Gamma}$ level (± 0.018) and V_{II} level (± 0.020) of the Rec-II-20ML SL. (e) The isosurfaces ($\pm 0.020 \times 2^{1/2}$) of the CB1-bottom and VB1-top WFs of a SL composed of alternating Rec-I and Rec-II interfaces. Note that the isosurface level is $2^{1/2}$ times larger than that used in (c) and (d) because the number of Rec-I (Rec-II) interfaces per unit cell is not two but one.

The interface electron state does not occur in the Rec-II SL, and neither in a Rec-I-like SL [Fig. 3(b)] that is constructed by removing O atoms from the Si-O-Si dimers of the Rec-II SL. The tetrahedral bonds of Si atoms near the Rec-I interface are distorted to form the Si-Si dimers, but the strains in the tetrahedral bonds are partially released when O atoms are inserted in the Si-Si dimers. This means that the distortion of tetrahedral bonds of Si atoms near the interface has a secondary effect on the formation of the interface state. Note that both the charge transfer induced by the bridging O atoms and the mixing of the orbitals of the O atoms are not dominant factors for the formation of the interface state. The role of the O atoms is just to keep the distance between the Si layers so as to interact with each other.

Interestingly, our finding that the interactions between the adjacent Si layers induce the interface electron state suggests that a similar interface state should be easily realized experimentally just by facing H-terminated reconstructed Si(001) substrates toward each other.

C. Origin of interface hole state

In the Rec-II interface, the O atoms are inserted in the Si-Si dimers. The coupling of the p_a orbitals of the inserted O atoms and those of the Si atoms induces the Rec-II interface hole state. The changes in geometry such as bond length and angle, charge transfer, and orbital coupling are reflected in the *ab initio* calculations. To evaluate the orbital coupling effect exclusively, we develop a nearest-neighbor tight-binding (TB) model as follows.

Since the tops of the valence bands of both Rec-I and Rec-II SLs are composed of almost p_a orbitals only, we ignore the other orbitals, and then expand the WF as

$$|\Psi^{(n\boldsymbol{k})}\rangle = \frac{1}{\sqrt{N}} \sum_i \sum_{\boldsymbol{R}} C_i^{(n\boldsymbol{k})} e^{i\boldsymbol{k}\cdot(\boldsymbol{R}+\boldsymbol{r}_i)} |\phi_{\mu(i)}(\boldsymbol{R}+\boldsymbol{r}_i)\rangle,$$

where n is the band index, $\boldsymbol{k}$ is the wave vector, N is the number of atoms in the unit cell, $C_i^{(n\boldsymbol{k})}$ is the expansion coefficient, $\boldsymbol{R}$ is the lattice vector, $\boldsymbol{r}_i$ is the position vector of the atom i, $\mu(i)$ indicates the atomic species (Si or O), and $\phi_{\mu(i)}$ indicates the p_a orbital of the atom $\mu(i)$.

The links of the interactions are illustrated in Fig. 4. The orbitals of the Si atoms of the Si-Si dimer couple each other. On the other hand, the orbitals of the Si atoms of the Si-O-Si dimer do not. Instead, those orbitals couple with the orbital of the inserted O atom. The difference in bond-network topology between the Rec-I and Rec-II SLs is thus taken into account.

The TB parameters are determined to reproduce the band structures calculated with the OpenMX and summarized in Table II. The parameters for Si are determined to reproduce the band structure of bulk Si as follows. The value of E_p(Si) is set to be 0.0 eV. The value of $V_{pp\pi}$(Si-Si) [$V_{pp\sigma}$(Si-Si)] is set to reproduce the difference in energy between the Γ'_{25} and X_4 (Γ_{15} and Γ'_{25}) levels [45]. Bulk Si and the Si layer can be regarded as being composed of a-directed zigzag chains of Si atoms. If the nearest-neighbor Si atoms i and j are in the same

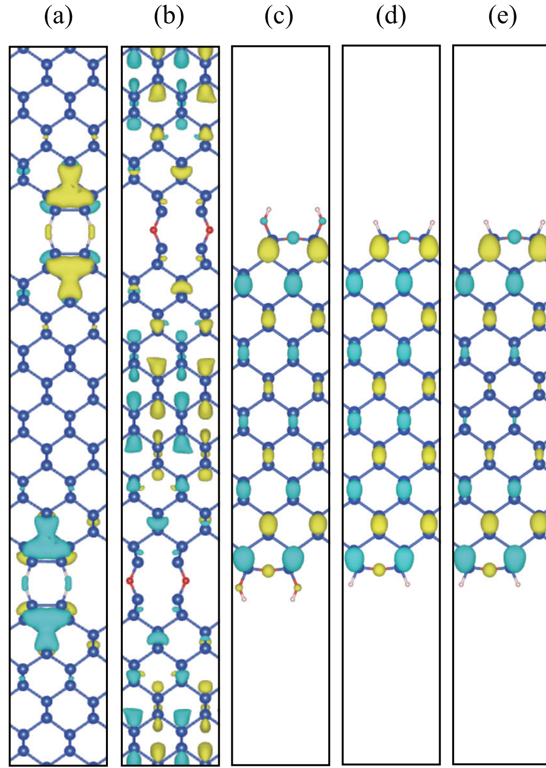

FIG. 3. (Color) Isosurfaces of WFs. (a) CB1-bottom of a pile of Si slabs with H-terminated Si-Si dimers (± 0.020). Note that the distance between H atoms of adjacent Si slabs is 0.85 Å. (b) CB1-bottom of the Rec-I-like SL (± 0.020). (c) VB1-top of the Si slab with OH-terminated Si-O-Si dimers ($\pm 0.020 \times 2^{1/2}$). (d) VB1-top of the Si slab with H-terminated Si-O-Si dimers ($\pm 0.020 \times 2^{1/2}$). (e) VB1-top of the hole-doped Si slab with H-terminated Si-O-Si dimers ($\pm 0.020 \times 2^{1/2}$). Note that the VB1-top level of the hole-doped Si slab is not occupied by electrons because holes are doped. The H atoms are placed 1.48 Å apart from the surface Si atoms or 1.00 Å apart from the O atoms. The structures are not optimized.

chain, the interaction energy between the p_a orbitals for bulk Si is

$$\langle \phi_{\mathrm{Si}}(\boldsymbol{r}_i)|H|\phi_{\mathrm{Si}}(\boldsymbol{r}_j)\rangle = \frac{2V_{pp\sigma}(\text{Si-Si}) + V_{pp\pi}(\text{Si-Si})}{3}.$$

On the other hand, if each nearest-neighbor Si atom is in a different chain,

$$\langle \phi_{\mathrm{Si}}(\boldsymbol{r}_i)|H|\phi_{\mathrm{Si}}(\boldsymbol{r}_j)\rangle = V_{pp\pi}(\text{Si-Si}).$$

We assume the same ones for Si atoms in SLs, whereby the difference in geometry such as bond length and angle is ignored. The value of $E_p(\text{O})$ is set to reproduce the difference in energy between the $3p$ orbital of an isolated Si atom and the $2p$ orbital of an isolated O atom. The value of $V^{(\text{I})}_{pp\pi}(\text{Si-O})$ is set to reproduce the difference in energy between the VB1(Z) and VB1(Γ) levels of the Rec-I-20ML SL. Here, the VB1(Z) level indicates the level of the VB1 band at the Z point. The value of $V^{(\text{II})}_{pp\pi}(\text{Si-O})$ ($= -1.488$eV), which is determined to reproduce the energy difference for the Rec-II-20ML SL, is different from that of $V^{(\text{I})}_{pp\pi}(\text{Si-O})$ ($= -1.759$eV). This difference primarily originates from the charge transfer. By fixing the value of $V_{pp\pi}(\text{Si-O})$, the charge transfer effect can be

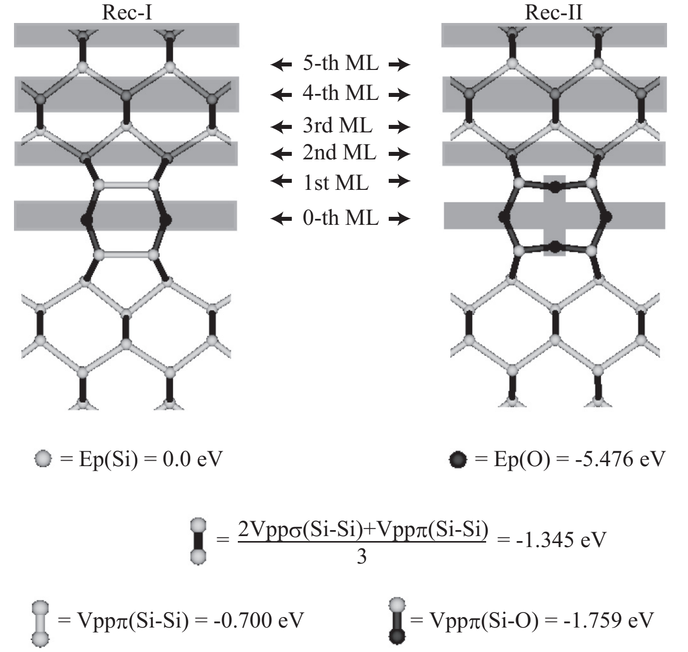

FIG. 4. Schematic representations of our TB model. The spheres and bonds represent on-site and hopping matrix elements, respectively. The ith MLs are defined by the gray and white regions.

ignored. Altogether, the effect of the coupling of the p_a orbitals can be exclusively examined by our TB model. Note that the results obtained by using $V^{((\text{I}))}_{pp\pi}(\text{Si-O})$ are shown below. The qualitatively same results are obtained by using $V^{(\text{II})}_{pp\pi}(\text{Si-O})$.

Figure 5 shows that the VB1-top level of the Rec-II-20ML SL is the interface state, while the VB1-top WF of the Rec-I-20ML SL delocalizes over the Si layer. Since our TB model qualitatively reproduces the results from the *ab initio* calculations, we conclude that the coupling of the p_a orbitals induces the Rec-II interface state.

The interface hole state also occurs in a Si slab with OH-terminated Si-O-Si dimers [Fig. 3(c)]. However, the degree of localization is lowered in a Si slab with H-terminated Si-O-Si dimers [Fig. 3(d)], in which less electrons are transferred from the surface Si atoms. However, when holes are doped (one electron per $\mathrm{Si_{40}O_4H_4}$ unit is removed), the degree of localization for the H-terminated Si slab increases [Fig. 3(e)]. These results indicate that the electron transfer induced by the bridging O atoms has a secondary effect on the formation of the Rec-II interface state. Moreover, our findings suggest that the locations of the channels of holes in a Si slab and a Si substrate also can be controlled by surface modification.

TABLE II. Parameters for our tight-binding model (in units of eV).

$E_p(\text{Si})$	0.000
$V_{pp\sigma}(\text{Si-Si})$	2.367
$V_{pp\pi}(\text{Si-Si})$	−0.700
$E_p(\text{O})$	−5.476
$V^{(\text{I})}_{pp\pi}(\text{Si-O})$	−1.759
$V^{(\text{II})}_{pp\pi}(\text{Si-O})$	−1.488

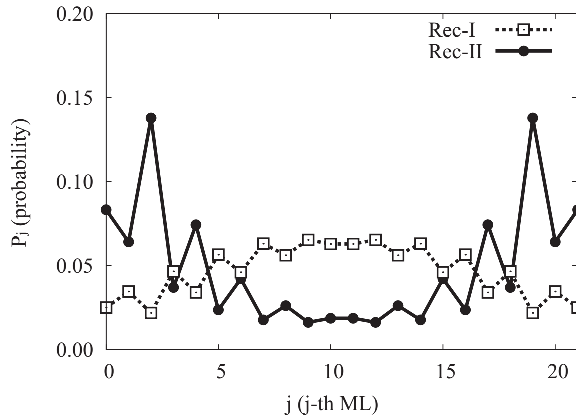

FIG. 5. Probability (P_j) that an electron of the VB1-top state is found in the jth ML. Here, $P_j = \sum_i l_{ij}|C_i|^2$. $l_{ij} = 1$ if the atom i is in the jth ML, otherwise $l_{ij} = 0$. C_i is the expansion coefficient for the p_a orbital of the atom i. The zeroth and 21st MLs are O MLs. The other MLs are Si MLs. P_j is normalized as $\sum_{j=0,20} P_j = 1$.

In a previous *ab initio* study [46], an interface hole state was found for a Si/quartz interface, but not found for a Si/cristobalite interface. From our findings, this result can be explained by the existence or nonexistence of Si-O-Si dimers at the Si/SiO_2 interface.

D. Transport properties

The Si/O/Si interface electron and hole states have the following three properties, which makes the Rec-I and Rec-II SLs attractive to be used for channel materials.

(i) The interface carriers have anisotropic effective masses, which is ideal for enhancing the carrier mobility along the channel ([110] direction) and reducing the gate-leakage current normal to the channel ([$\bar{1}$10] direction) as follows.

(a) The interface carriers have small effective masses along the [110] direction as shown in Table III, being ideal for enhancing the carrier mobility. Specifically, for the electrons in the Rec-I-4ML and Rec-I-20ML SLs, the effective masses of CB1 in the [110] direction ($m^{\rm CB1}_{[110]}$) are 0.12 and 0.14 $m_{\rm e}$, respectively. Here, $m_{\rm e}$ is the electron mass. The calculated values are smaller than the electron effective mass obtained for strained Si (s-Si) under 2 GPa uniaxial tensile stress in the [110] direction: 0.16 $m_{\rm e}$. Similarly, for the holes in the Rec-II-4ML and Rec-II-20ML SLs, the values of $m^{\rm VB1}_{[110]}$ are 0.09 and 0.11 $m_{\rm e}$, respectively. These are smaller than or comparable to the hole effective mass of s-Si under 2 GPa uniaxial compressive stress in the [110] direction: 0.11 $m_{\rm e}$. The [110] direction is the best suited direction toward which the channel is oriented because both electrons and holes in the SLs take the smallest effective mass (see the Supplemental Material for details [30]).

(b) The interface carriers have large effective masses in the direction normal to the [110] direction, being ideal for reducing the gate-leakage current [13]. Specifically, for the electrons in the Rec-I-4ML (Rec-I-20ML) SL, $m^{\rm CB1}_{[\bar{1}10]}$ and $m^{\rm CB1}_{[001]}$ are 2.18 and 2.09 $m_{\rm e}$ (0.38 and 2.53 $m_{\rm e}$), respectively. These are much larger than $m^{\rm CB1}_{[110]}$: 0.12 $m_{\rm e}$ (0.14 $m_{\rm e}$). Similarly, for the holes in the Rec-II-4ML (Rec-II-20ML) SL, $m^{\rm VB1}_{[\bar{1}10]}$ and $m^{\rm VB1}_{[001]}$ are 1.82 and 0.74 $m_{\rm e}$ (2.88 and 0.40 $m_{\rm e}$), respectively. These are much larger than $m^{\rm VB1}_{[110]}$: 0.09 $m_{\rm e}$ (0.11 $m_{\rm e}$).

(ii) Most electrons (holes) occupy the interface state, allowing us to make the best use of the small effective mass of the interface state, because the energy splitting $\Delta E_{\rm CB} \equiv |E_{\rm CB2} - E_{\rm CB1}|$ ($\Delta E_{\rm VB} \equiv |E_{\rm VB2} - E_{\rm VB1}|$) is much larger than $k_{\rm B}T$ at room temperature: 26 meV. Here, $E_{{\rm CB}i}$ ($E_{{\rm VB}i}$) is the energy at the bottom of the ith lowest conduction band CBi (top of the ith highest valence band VBi). $k_{\rm B}$ and T are Boltzmann constant and room temperature (300 K), respectively. Furthermore, the value of $\Delta E_{\rm CB}$ ($\Delta E_{\rm VB}$) is expected to increase due to the quantum confinement when the gate bias is applied because $r^{\rm CB}_{[\bar{1}10]}, r^{\rm CB}_{[001]} > 1$ ($r^{\rm VB}_{[\bar{1}10]}, r^{\rm VB}_{[001]} > 1$) [13]. Here, $r^{\rm CB}_{[\bar{1}10]} \equiv m^{\rm CB1}_{[\bar{1}10]}/m^{\rm CB2}_{[\bar{1}10]}$.

(iii) The interface states are nondegenerated, being ideal for reducing the interband scattering [12].

TABLE III. Properties of the electrons and holes in the epitaxial Si/O SLs. The effective masses are given in units of electron mass. The energy splittings are given in units of meV. For comparison purpose, the results for s-Si under ∓2 GPa uniaxial stress in the [110] direction are also shown. For s-Si, $\Delta E_{\rm CB} \equiv |E_{\rm CB3} - E_{\rm CB1}|$ and $r^{\rm CB}_{[\bar{1}10]} \equiv m^{\rm CB1}_{[\bar{1}10]}/m^{\rm CB3}_{[\bar{1}10]}$ because CB1 and CB2 are degenerated.

Electron	$m^{\rm CB1}_{[110]}$	$m^{\rm CB1}_{[\bar{1}10]}$	$m^{\rm CB1}_{[001]}$	$\Delta E_{\rm CB}$	$r^{\rm CB}_{[\bar{1}10]}$	$r^{\rm CB}_{[001]}$
Rec-I-4ML	0.12	2.18	2.09	780	6.4	7.5
Rec-I-20ML	0.14	0.38	2.53	97	1.9	1.7
s-Si (-2GPa)	0.16	0.25	1.04	104	0.8	5.4
hole	$m^{\rm VB1}_{[110]}$	$m^{\rm VB1}_{[\bar{1}10]}$	$m^{\rm VB1}_{[001]}$	$\Delta E_{\rm VB}$	$r^{\rm VB}_{[\bar{1}10]}$	$r^{\rm VB}_{[001]}$
Rec-II-4ML	0.09	1.82	0.74	801	3.6	1.2
Rec-II-20ML	0.11	2.88	0.40	132	1.2	6.4
s-Si (+2GPa)	0.11	1.90	0.27	115	15.0	1.2

E. Quantum confinement effects

The localization of the electrons and holes around the interfaces is somehow unexpected and contrary to Tsu's expectations [22]. However, this does not imply that there is no quantum confinement effect in the Si/O SLs. Actually, the quantum confinement effects impact on the electronic states whose WFs delocalize over the Si layers. Interestingly, unlike for the nanostructures embedded in thick insulating layers, the impact of the quantum confinement induced by the Si/O/Si interfaces depends on the symmetry matching between the WF and the interface structure. The WFs of the V_a and V_b levels of the Rec-I-20ML SL are characterized by zigzag chains of p orbitals along the a and b directions, respectively [Fig. 2(c)]. These two levels are degenerated in bulk Si. In the SL, however, the V_a level lies 94 meV above the V_b level due to the symmetry-dependent quantum confinement effect. The b-directed chains do not match the five-membered rings of the interfaces. Therefore, the V_b WF cannot penetrate through the interface and is confined in the Si layers. On the other hand, the a-directed chains match the symmetry of the interface so that, although the amplitude is decreased

around the interface, the V_a WF penetrates through it, and the electronic states of the adjacent Si layers couple each other. Due to the coupling, the energy of the VB1, to which the V_a level belongs, increases as it goes from the Γ point to the Z point in the Brillouin zone.

For reference, we show the band structures of H-terminated 20ML-Si slabs in Appendix D. The band gaps (E_gs) of Si nanostructures are usually higher than the E_g of bulk Si due to quantum-confinement effects [1–10]. Actually, the E_gs of the 20 ML Si slabs with H-terminated Si-Si dimers (0.80 eV), OH-terminated Si-Si dimers (0.74 eV), H-terminated nonreconstructed surface (0.78 eV) are larger than the E_g of bulk Si (0.62 eV in our simulation scheme). Contrary to the conventional Si nanostructures, the E_gs of the Rec-I-20ML SL (0.63 eV) and the Rec-II-20ML SL (0.50 eV) are comparable to and smaller than the E_g of bulk Si, respectively. This is because the interface states are not influenced by the quantum-confinement effects. Similarly, the E_g of the 20 ML Si slab with OH-terminated Si-O-Si dimers (0.56 eV) is smaller than that of bulk Si. The E_g of the 20ML Si slab with H-terminated Si-O-Si dimers (0.64 eV) is larger than that of the OH-terminated Si slab because of the weaker localization in the H-terminated Si slab. We also note that the Rec-I-20ML SL has a direct band gap. However, the radiative recombination rate, 41 s^{-1}, is small because the WFs of the C_I and V_a levels do not overlap well each other. For reference, the rates for H-terminated Si nanodots of 2.4 nm in diameter [8] are more than 10^3 s^{-1}.

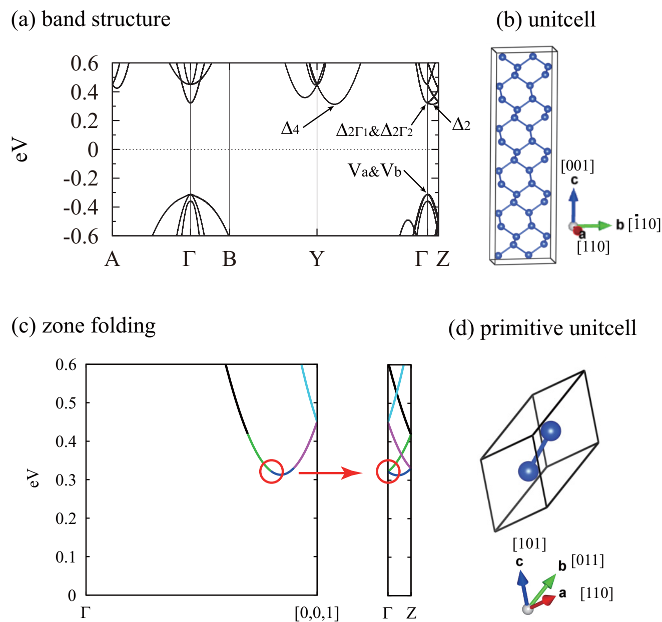

FIG. 6. (Color online) (a) Band structure of bulk Si calculated using a unit cell shown in (b). Note that $A = \frac{2\pi}{l_b}(\frac{1}{2},\frac{1}{2},0) \equiv [\frac{1}{2},\frac{1}{2},0]$, $\Gamma = [0,0,0]$, $B = [-\frac{1}{4},\frac{1}{4},0]$, $Y = [0,1,0]$, and $Z = [0,0,\frac{1}{10}]$, where l_b is the lattice constant of bulk Si. These points are not necessarily in the first Brillouin zone. (c) Zone folding. Left panel is the band structure of bulk Si calculated using the primitive unit cell shown in (d). Right panel is the band structure calculated using the unit cell shown in (b).

F. Large valley splitting

Another interesting consequence of the quantum confinement effect on the Rec-II-20ML SL consists in the energy splitting of the sixfold conduction band minimum of bulk Si, being ideal for developing Si-based qubits [47]. Since the electron effective masses along the z direction of the fourfold in-plane Δ_4 valleys are smaller than those of the twofold out-of-plane Δ_2 valleys, the increases in energy of the Δ_4 valleys due to the quantum confinement are larger than those of the Δ_2 valleys. The lower-energy Δ_2 valleys further split into $\Delta_{2\Gamma}$ and Δ_{2Z} valleys due to the valley-valley coupling [47]. The splitting for Si nanostructures is usually small (at most 1 meV [48]), which prevents developing Si-based qubits. For

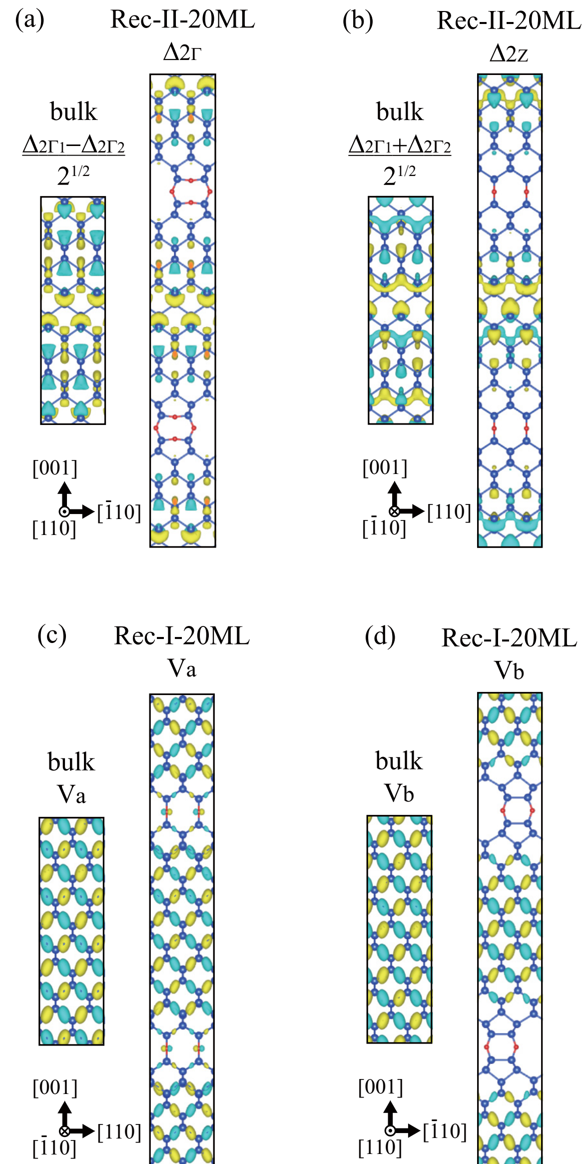

FIG. 7. (Color online) Comparison of WFs of bulk Si (Ψ) and epitaxial Si/O SLs (Φ). Isosurfaces of (a) $(\Psi_{\Delta_{2\Gamma_1}} - \Psi_{\Delta_{2\Gamma_2}})/2^{1/2}$ and $\Phi_{\Delta_{2\Gamma}}$, (b) $(\Psi_{\Delta_{2\Gamma_1}} + \Psi_{\Delta_{2\Gamma_2}})/2^{1/2}$ and $\Phi_{\Delta_{2Z}}$, (c) Ψ_{V_a} and Φ_{V_a}, and (d) Ψ_{V_b} and Φ_{V_b}. ±0.021 isosurfaces for $(\Psi_{\Delta_{2\Gamma_1}} - \Psi_{\Delta_{2\Gamma_2}})/2^{1/2}$ and $(\Psi_{\Delta_{2\Gamma_1}} + \Psi_{\Delta_{2\Gamma_2}})/2^{1/2}$, ±0.018 for $\Phi_{\Delta_{2\Gamma}}$ and $\Phi_{\Delta_{2Z}}$, ±0.020 for Ψ_{V_a}, Ψ_{V_b}, Φ_{V_a}, and Φ_{V_b} are shown.

the Rec-II-20ML SL, however, the magnitude of the energy splitting is 15.3 meV (see the Supplemental Material for the accuracy [30]). This value is larger than the reported values for a 20ML Si well embedded in Ge (2 meV) and for a 40ML Si well embedded in an optimal Si/Ge SL (8.7 meV) [47].

We also investigate the valley splitting in Si slabs. The values for the 20ML Si slabs with OH-terminated Si-O-Si dimers (12.2 meV), H-terminated Si-O-Si dimers (11.0 meV), and OH-terminated Si-Si dimers (11.8 meV) are larger than those for H-terminated Si-Si dimers (2.1 meV) and H-terminated nonreconstructed surface (0.1 meV). These results imply that the surface oxidation enhances the valley splitting. The formation of Si-O bonds near Si/SiO_2 interfaces might play an important role for the 23-meV large splitting observed in a $SiO_2/Si(001)/SiO_2$ quantum well [49].

IV. CONCLUSION

To conclude, using geometrical considerations and *ab initio* calculations, we have shown that our Rec-I and Rec-II Si/O SL models are energetically more favorable than all the models proposed so far. Our Si/O/Si interface models are composed of reconstructed Si{001} surfaces connected by Si-O-Si bridges, which allows each atom to maintain its natural bonding configuration. The part of the Rec-II interface is experimentally accessible just by oxidizing a Si(001) substrate. To complete the Rec-II superlattice, we have proposed a three-step method. We have also explored the potential of our Si/O superlattice models for new materials used in future Si electronics. To our surprise, the Rec-I and Rec-II interfaces create the interface electron and hole states, respectively. The Rec-I interface state originates from the interactions between the adjacent Si layers. This indicates that similar interface states should be easily realized experimentally just by facing H-terminated reconstructed Si(001) substrates toward each other or by stacking Si slabs with H-terminated Si-Si dimers. On the other hand, the p_a orbitals of O atoms inserted in the Si-Si dimers induce the Rec-II interface state. This indicates that the locations of channels of holes in a Si slab and a Si substrate can be controlled by surface modification as well. Interestingly, the Rec-I and Rec-II interface carriers have small effective masses in the direction parallel to the channel ([110] direction) and large effective masses in the direction normal to the channel ([$\bar{1}$10] direction), making the Si/O superlattices attractive to be used for channel materials. We have also shown that the valley splitting of Si is enhanced by the formation of the Si/O/Si interfaces, being ideal for developing Si based qubits. Our findings open new perspectives to design and control the electronic properties of Si.

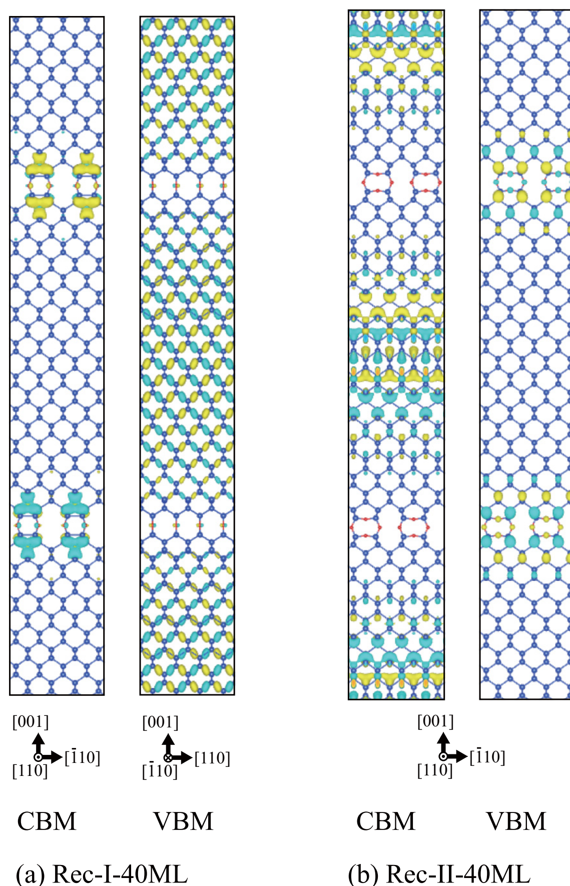

FIG. 8. (Color online) Isosurfaces of CBM and VBM WFs. (a) Epitaxial Rec-I-40ML superlattice. ± 0.020 and $\pm 0.020/2^{1/2}$ isosurfaces are shown for the CBM and VBM WFs, respectively. (b) Epitaxial Rec-II-40ML superlattice. $\pm 0.018/2^{1/2}$ and ± 0.020 isosurfaces are shown for the CBM and VBM WFs, respectively.

ACKNOWLEDGMENTS

This work is supported by AIST-IMEC collaboration project. K.N. wishes to thank T. Ozaki, N. Orita, and S. Ishibashi for fruitful discussions. GDIS [50] was used to generate the atomic arrangements. VESTA [51] was used to illustrate isosurfaces of WFs.

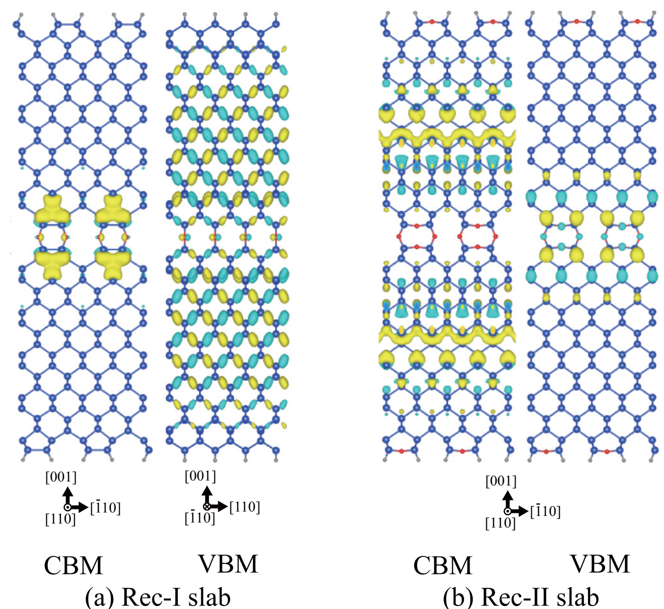

FIG. 9. (Color online) Isosurfaces of CBM and VBM WFs. (a) Rec-I slab. $\pm 0.020 \times 2^{1/2}$ and ± 0.020 isosurfaces are shown for the CBM and VBM WFs, respectively. (b) Rec-II slab. ± 0.018 and $\pm 0.020 \times 2^{1/2}$ isosurfaces are shown for the CBM and VBM WFs, respectively.

APPENDIX A: BAND STRUCTURE AND WAVE FUNCTIONS OF BULK SI

The band structure of bulk Si calculated using a unit cell containing 20 ML of Si is shown in Fig. 6(a). The conduction band minimum of bulk Si is sixfold, namely, the Δ_2 and Δ_4 levels are degenerated. The $\Delta_{2\Gamma_1}$ and $\Delta_{2\Gamma_2}$ levels, which are the twofold lowest energy levels of the conduction band at Γ, are folded from the $\frac{2\pi}{l_b}(0,0,\pm\frac{8}{10})$ points of the band structure calculated using the primitive unit cell [Figs. 6(c) and 6(d)].

Figures 7(a) and 7(b) show that the $\Delta_{2\Gamma}$ and Δ_{2Z} levels of the Rec-II-20ML SL originate from the $\Delta_{2\Gamma_1}$ and $\Delta_{2\Gamma_2}$ levels of bulk Si, respectively. Actually, $\Phi_{\Delta_{2\Gamma}}$ and $\Phi_{\Delta_{2Z}}$ resemble to $(\Psi_{\Delta_{2\Gamma_1}} - \Psi_{\Delta_{2\Gamma_2}})/2^{1/2}$ and $(\Psi_{\Delta_{2\Gamma_1}} + \Psi_{\Delta_{2\Gamma_2}})/2^{1/2}$, respectively. Here, $\Phi_{\Delta_{2\Gamma}}$ ($\Phi_{\Delta_{2Z}}$) is the WF of the $\Delta_{2\Gamma}$ (Δ_{2Z}) level of the Rec-II-20ML SL and $\Psi_{\Delta_{2\Gamma_1}}$ ($\Psi_{\Delta_{2\Gamma_2}}$) is the WF of the $\Delta_{2\Gamma_1}$ ($\Delta_{2\Gamma_2}$) level of bulk Si. Note that the molecular orbitals of the adjacent Si layers in the $\Phi_{\Delta_{2\Gamma}}$ are in phase because the $\Delta_{2\Gamma}$ level is located at the Γ point. On the other hand, the molecular orbitals of the adjacent Si layers in the $\Phi_{\Delta_{2Z}}$ are out of phase because the Δ_{2Z} level is located at the Z point. Figures 7(c) and 7(d) also show that the V_a and V_b levels of the Rec-I-20ML SL originate from the V_a and V_b levels of bulk Si, respectively.

APPENDIX B: WAVE FUNCTIONS OF THE REC-I-AND REC-II-40ML SUPERLATTICES

The WFs of the epitaxial Rec-I- and Rec-II-40ML SLs were calculated using Si7.0-$s2p2d1$ and O5.0-$s2p2d1$ basis sets, and are shown in Fig. 8. The atomic positions are optimized using an out-of-plane unit-cell vector $\boldsymbol{c} = (-\frac{l_b}{4}, \frac{l_b}{4}, c_{z20\text{ML}} + 5l_b)$. Here, $c_{z20\text{ML}}$ is the calculated z component of $\boldsymbol{c}$ for the corresponding 20ML SL.

The conduction-band-minimum (CBM) WF of the Rec-I-40ML SL is localized around the Rec-I interface, while the valence-band-maximum (VBM) WF delocalizes over the Si layers. For the Rec-II-40ML SL, reversely, the VBM WF is localized around the Rec-II interface, while the CBM WF delocalizes over the Si layers.

APPENDIX C: WAVE FUNCTIONS OF SLAB MODELS HAVING ONE SI/O/Si INTERFACE

The WFs of isolated slabs composed of one Si/O/Si interface between two Si layers are shown in Fig. 9. Each Si layer consists of 20 MLs of Si. The surface dangling bonds are terminated by hydrogen to remove the dangling-bond states from the band gap. The H atoms are placed 1.4 Å apart from surface Si atoms, but the atomic positions are not optimized.

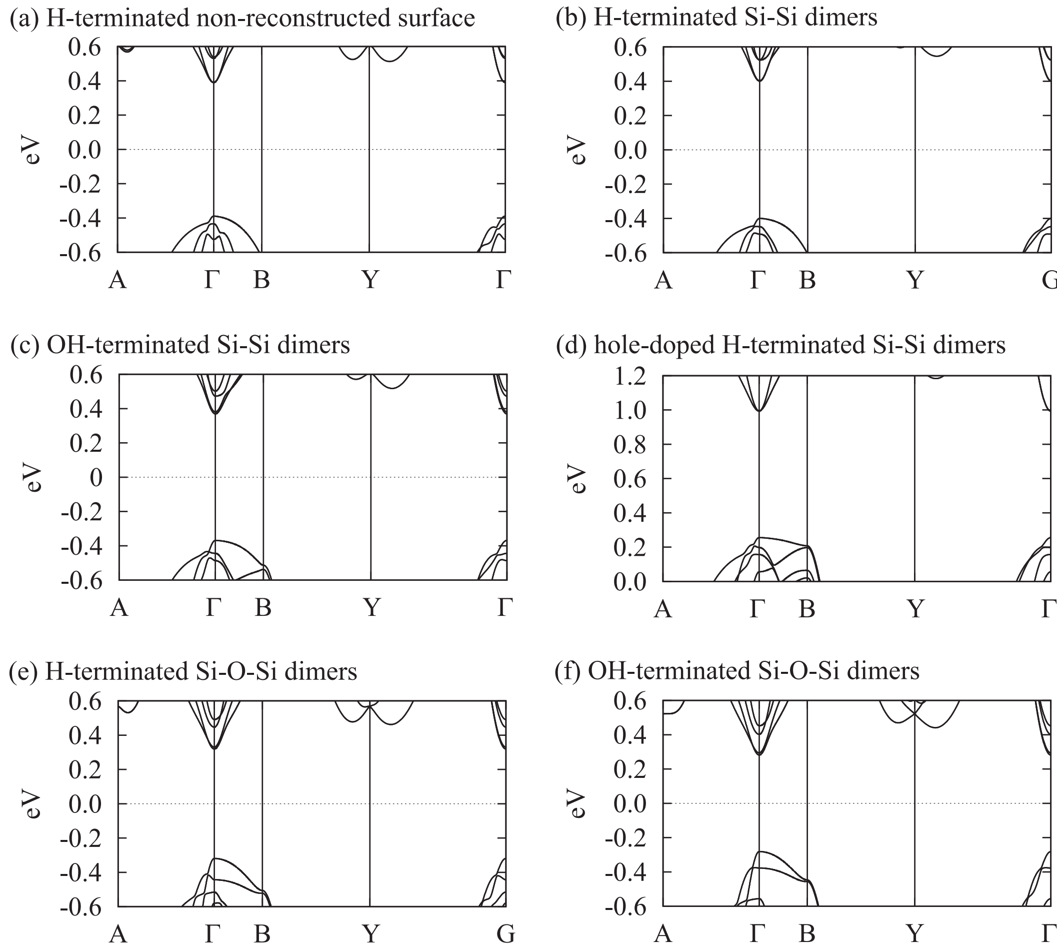

FIG. 10. Band structures of 20ML Si slabs with (a) H-terminated non-reconstructed surface, (b) H-terminated Si-Si dimers, (c) OH-terminated Si-Si dimers, (d) hole-doped H-terminated Si-Si dimers: one electron per $Si_{40}O_4H_4$ unit is removed, (e) H-terminated Si-O-Si dimers, and (f) OH-terminated Si-O-Si dimers.

Note that, in Appendix D, the H atoms are placed 1.48 Å apart from surface Si atoms, but the small difference in Si-H bond length does not affect the results.

The CBM WF of the Rec-I slab is localized around the Rec-I interface, while the VBM WF delocalizes over the Si layers. For the Rec-II slab, reversely, the VBM WF is localized around the Rec-II interface, while the CBM WF delocalizes over the Si layers. These results show that the formation of one Si/O/Si interface is enough to create the interface channel.

APPENDIX D: BAND STRUCTURES OF H-TERMINATED 20 ML SI SLABS

The band structures of 20ML Si slabs are shown in Fig. 10. The structure models are constructed by cutting out bulk Si, Rec-I-20ML SL, or Rec-II-20ML SL. The H atoms are placed 1.48 and 1.00 Å apart from surface Si and O atoms, respectively. Note that each surface Si atom of nonreconstructed surface has two Si-H bonds.

[1] H. Takagi, H. Ogawa, Y. Yamazaki, A. Ishizaki, and T. Nakagiri, Appl. Phys. Lett. **56**, 2379 (1990).
[2] L. T. Canham, Appl. Phys. Lett. **57**, 1046 (1990).
[3] A. G. Cullis, L. T. Canham, and P. D. J. Calcott, J. Appl. Phys. **82**, 909 (1997).
[4] D. J. Lockwood, Z. H. Lu, and J.-M. Baribeau, Phys. Rev. Lett. **76**, 539 (1996).
[5] Z. H. Lu and D. Grozea, Appl. Phys. Lett. **80**, 255 (2002).
[6] N. Tit and M. Dharma-wardana, Solid State Commun. **106**, 121 (1998).
[7] P. Carrier, L. J. Lewis, and M. W. C. Dharma-wardana, Phys. Rev. B **65**, 165339 (2002).
[8] K. Nishio, J. Kōga, T. Yamaguchi, and F. Yonezawa, Phys. Rev. B **67**, 195304 (2003).
[9] Y. Kanemitsu, Phys. Rep. **263**, 1 (1995).
[10] H. Kageshima, Surf. Sci. **357-358**, 312 (1996).
[11] C. S. Smith, Phys. Rev. **94**, 42 (1954).
[12] D. K. Nayak and S. K. Chun, Appl. Phys. Lett. **64**, 2514 (1994).
[13] S. Thompson, G. Sun, Y. S. Choi, and T. Nishida, IEEE Trans. Electron Devices **53**, 1010 (2006).
[14] Z. Liu, J. Wu, W. Duan, M. G. Lagally, and F. Liu, Phys. Rev. Lett. **105**, 016802 (2010).
[15] M. Zhou, Z. Liu, Z. Wang, Z. Bai, Y. Feng, M. G. Lagally, and F. Liu, Phys. Rev. Lett. **111**, 246801 (2013).
[16] M. Fornari, Physics **6**, 140 (2013).
[17] G. L. W. Hart, S. Curtarolo, T. B. Massalski, and O. Levy, Phys. Rev. X **3**, 041035 (2013).
[18] K. Koga, G. T. Gao, H. Tanaka, and X. C. Zeng, Nature (London) **412**, 802 (2001).
[19] K. Takeda and K. Shiraishi, Phys. Rev. B **50**, 14916 (1994).
[20] P. Vogt, P. De Padova, C. Quaresima, J. Avila, E. Frantzeskakis, M. C. Asensio, A. Resta, B. Ealet, and G. Le Lay, Phys. Rev. Lett. **108**, 155501 (2012).
[21] A. Fleurence, R. Friedlein, T. Ozaki, H. Kawai, Y. Wang, and Y. Yamada-Takamura, Phys. Rev. Lett. **108**, 245501 (2012).
[22] R. Tsu, Nature (London) **364**, 19 (1993).
[23] R. Tsu and J. C. Lofgren, J. Cryst. Growth **227-228**, 21 (2001).
[24] K. Dovidenko, J. Lofgren, F. de Freitas, Y. Seo, and R. Tsu, Physica E **16**, 509 (2003).
[25] R. J. Mears, M. Hytha, I. Dukovski, A. Yiptong, X. Huang, S. Halilov, A. Broka, R. J. Stephenson, V. Rao, D. R. Webb, R. Prasad, S. A. Kreps, H. Takeuchi, S. Ikeda, G. Gebara, K. Matthews, J. Wetzel, W. Xiong, C. Bowen, R. Wise, and C. R. Cleavelin, in *Proceedings of the IEEE International SOI Conference* (IEEE, New York, 2007), pp. 23–24.
[26] A. Delabie, S. Jayachandran, M. Caymax, R. Loo, J. Maggen, G. Pourtois, B. Douhard, T. Conard, J. Meersschaut, H. Lenka, W. Vandervorst, and M. Heyns, ECS Solid State Lett. **2**, P104 (2013).
[27] X. Luo, S. B. Zhang, and S.-H. Wei, Phys. Rev. Lett. **89**, 076802 (2002).
[28] R. M. Tromp, R. J. Hamers, and J. E. Demuth, Phys. Rev. Lett. **55**, 1303 (1985).
[29] Y. Tu and J. Tersoff, Phys. Rev. Lett. **84**, 4393 (2000).
[30] See Supplemental Material at http://link.aps.org/supplemental/10.1103/PhysRevB.91.165303 for details in geometry optimization, accuracy of valley-splitting energy, and anisotropic effective masses.
[31] http://qmas.jp/.
[32] J. P. Perdew, K. Burke, and M. Ernzerhof, Phys. Rev. Lett. **77**, 3865 (1996).
[33] P. E. Blöchl, Phys. Rev. B **50**, 17953 (1994).
[34] A. Ourmazd, D. W. Taylor, J. A. Rentschler, and J. Bevk, Phys. Rev. Lett. **59**, 213 (1987).
[35] A. Pasquarello, M. S. Hybertsen, and R. Car, Phys. Rev. Lett. **74**, 1024 (1995).
[36] T. Yamasaki, C. Kaneta, T. Uchiyama, T. Uda, and K. Terakura, Phys. Rev. B **63**, 115314 (2001).
[37] H. Kageshima, M. Uematsu, K. Akagi, S. Tsuneyuki, T. Akiyama, and K. Shiraishi, e-J. Surf. Sci. Nanotech. **4**, 584 (2006).
[38] N. Ikarashi, K. Watanabe, and Y. Miyamoto, Phys. Rev. B **62**, 15989 (2000).
[39] M. M. Roberts, L. J. Klein, D. E. Savage, K. A. Slinker, M. Friesen, G. Celler, M. A. Eriksson, and M. G. Lagally, Nature Mater. **5**, 388 (2006).
[40] http://www.openmx-square.org/
[41] N. Troullier and J. L. Martins, Phys. Rev. B **43**, 1993 (1991).
[42] A. H. MacDonald and S. H. Vosko, J. Phys. C **12**, 2977 (1979).
[43] G. B. Bachelet, D. R. Hamann, and M. Schlüter, Phys. Rev. B **26**, 4199 (1982).
[44] G. Theurich and N. A. Hill, Phys. Rev. B **64**, 073106 (2001).
[45] W. A. Harrison and Physics, *Electronic Structure and the Properties of Solids: The Physics of the Chemical Bond* (Dover Publications, New York, 1989).
[46] Y. Suwa and S.-i. Saito, Phys. Rev. B **79**, 233308 (2009).
[47] L. Zhang, J.-W. Luo, A. Saraiva, B. Koiller, and A. Zunger, Nature Commun. **4**, 2396 (2013).
[48] F. Zwanenburg, A. Dzurak, A. Morello, M. Simmons, L. Hollenberg, G. Klimeck, S. Rogge, S. Coppersmith, and M. Eriksson, Rev. Mod. Phys. **85**, 961 (2013).
[49] K. Takashina, Y. Ono, A. Fujiwara, Y. Takahashi, and Y. Hirayama, Phys. Rev. Lett. **96**, 236801 (2006).
[50] http://gdis.sourceforge.net/index.html/.
[51] K. Momma and F. Izumi, J. Appl. Crystallogr. **44**, 1272 (2011).